sustainability

MDPI

Article

Preparation of Fe-Based MOFs Composite as an Adsorptive Photocatalyst with Enhanced Photo-Fenton Degradation under LED Light Irradiation

Patrick Armando [1], Valentino Bervia Lunardi [1], Felycia Edi Soetaredjo [1], Jindrayani Nyoo Putro [1], Shella Permatasari Santoso [1], Christian Julius Wijaya [1], Jenni Lie [1], Wenny Irawaty [1], Maria Yuliana [1], Hardy Shuwanto [2], Hairus Abdullah [2], I Gede Wenten [3] and Suryadi Ismadji [1,*]

[1] Department of Chemical Engineering, Widya Mandala Surabaya Catholic University, Kalijudan 37, Surabaya 60114, Indonesia
[2] Department of Industrial Engineering, Universitas Prima Indonesia, Medan 20117, Indonesia
[3] Department of Chemical Engineering, Institute of Technology Bandung (ITB), Jl. Ganesha 10, Bandung 40132, Indonesia
* Correspondence: suryadiismadji@yahoo.com; Tel.: +62-31-3891264

Abstract: In this study, a novel MIL-100(Fe)@TiO_2 composite was synthesized and used as the adsorbent to remove Rhodamine B from synthetic wastewater through adsorption and photocatalytic degradation. The composite was synthesized successfully using solvothermal methods. MIL-100(Fe)@TiO_2 composite has excellent adsorption and photodegradation capability for Rhodamine B removal. The reusability of the materials was observed, with the conclusion that the material still had good adsorption and photocatalytic performance after five cycles of consecutive experiments. The adsorption isotherm, kinetic, and thermodynamic studies of the removal of Rhodamine B were also conducted. The Langmuir model represented the adsorption equilibrium data better than other models. The kinetics of adsorption of Rhodamine B was presented well by pseudo-first-order. The thermodynamic study verified that the physisorption mechanism was more dominant than chemisorption. The addition of Fenton was also proven to be successful in increasing the photocatalytic abilities of the synthesized materials.

Keywords: metal–organic framework; photocatalytic degradation; thermodynamic; composite

Citation: Armando, P.; Lunardi, V.B.; Edi Soetaredjo, F.; Putro, J.N.; Santoso, S.P.; Wijaya, C.J.; Lie, J.; Irawaty, W.; Yuliana, M.; Shuwanto, H.; et al. Preparation of Fe-Based MOFs Composite as an Adsorptive Photocatalyst with Enhanced Photo-Fenton Degradation under LED Light Irradiation. *Sustainability* **2022**, *14*, 10685. https://doi.org/10.3390/su141710685

Academic Editor: Ning Yuan

Received: 28 June 2022
Accepted: 24 August 2022
Published: 27 August 2022

1. Introduction

An emerging three-dimensional porous crystalline framework class, metal–organic frameworks (MOFs), exhibits ordered pore size and surface area, which is beneficial for catalytic application [1]. MOF outperforms conventional photocatalytic semiconductor materials in several factors such as framework versatility, huge surface area, and more significant void volumes. Currently, MOFs have been widely utilized as novel types of photocatalysts. This is due to the availability of electrons to be excited from the highest occupied molecular orbital (HOMO) to the lowest unoccupied molecular orbital (LUMO) due to LMCT (ligand-to-metal charge transfer), MLCT (metal-to-ligand charge transfer), and π-π^* transition in aromatic rings' properties when exposed to light irradiation [2]. Fe-based MOFs are presented as high-grade photocatalysts among constructed MOFs due to their intrinsic optical absorbance, stability, inherent optical responsiveness, and low-cost synthesis [3]. Moreover, they have been demonstrated to be effective heterogeneous photo-Fenton-like, to produce OH radicals for the degradation of organic pollutants. However, the poor adsorption ability towards dye molecules [4,5] and low efficiency of excitation electron production and MOFs charge separation, contribute to limited efficiency in the photocatalytic system [6,7]. Therefore, a pristine MOFs photocatalyst cannot provide sufficient catalytic degrading efficiency and stability.

In recent years, the plausible strategy of improving MOFs photocatalytic activity was proven by incorporating semiconductors into MOFs. Amid a wide inorganic semiconductor selection, TiO_2@MOFs surpass their counterparts in terms of a synergistic impact of high adsorption and efficient charge excitation and transfer. For instance, Huang et al. [8] reported that the impregnation of N-TiO_2 nanoparticles on MIL-100 (Fe) provides a great synergistic effect through electron-hole recombination restriction, along with suitable pore size and high surface area for promoting the photocatalytic reaction for methylene blue degradation [8]. In another study, He et al. [9] introduced MIL-100 (Fe) on the P-25 matrix to extend the light absorption ability to the visible region for efficiency degradation improvement against heavy metals [9]. Moreover, Liu et al. [10] engineered a hierarchical sandwich consisting of TiO_2 nanosheets and porous MIL-100 (Fe) to improve composite adsorption ability and limit the recombination of photo-generated e^-/h^+ pairs to promote the photocatalytic activity against methylene blue under visible light irradiation. The interfaces between TiO_2 semiconductors and MOFs provide many suitable sites for photo-generated electron transition, which significantly speeds up electron transfer and reduces electron-hole recombination. Additionally, the aggregation tendency of pristine TiO_2 can also be overcome by anchoring the MIL-100(Fe) on the TiO_2 surface. However, no study exploits the possibility of TiO_2 anatase for MIL-100(Fe) composite. Based on the structural configuration, TiO_2 anatase provides a unique structure with numerous defects that can confine high oxygen content for electron confinement [11].

In this study, we prepared novel photocatalyst Fe-based MOFs (MIL-100(Fe)) grown on the TiO_2 anatase surface to enhance the adsorption and photocatalytic degradation of dyes with the assistance of H_2O_2 and visible light. This paper selected rhodamine B (RhB) as a target emerging organic pollutant, to evaluate the adsorption and photo-Fenton performance of MIL-100(Fe)@TiO_2. Several adsorption isotherm and kinetic models were utilized to provide the insight mechanism of adsorption of RhB on the composites. Meanwhile, several process parameters such as catalyst ratio, catalyst dosage, and H_2O_2 content, which were co-existing inorganic anions on photo-Fenton degradation of RhB, were evaluated with an additional study regarding the stability and recyclability performance of MIL-100(Fe)@anatase TiO_2. A plausible mechanism for photocatalytic degradation of RhB via LED irradiation by MIL-100(Fe)@TiO_2 has been proposed.

2. Materials and Methods

2.1. Chemicals

The chemicals used in this study were ferric nitrate hexahydrate ($Fe(NO_3)_3{\cdot}9H_2O$) (CAS:7782-61-8, 99.95% purity trace metal basis), 1,3,5-Benzene Tricarboxylic Acid (H_3BTC) (CAS: 554-95-0; 98%), Titanium (IV) oxide (TiO_2) (CAS: 1317-70-10) anatase grade, 99.8% trace metal basis), rhodamine B ($C_{28}H_{31}ClN_2O_3$) (CAS:548-62-9; HPLC standard $\geq$ 95% anhydrous basis), isopropyl alcohol (IPA) (CAS:67-63-0; ACS reagent $\geq$ 99.5%), *P*-benzoquinone ($C_6H_4O_2$) (CAS:106-51-4; reagent grade $\geq$ 99.5%), carbon tetrachloride (CCl_4) (CAS: 56-23-5; reagent grade $\geq$ 99.9%) and ammonium oxalate monohydrate ($(NH_4)_2C_2O_4{\cdot}H_2O$) (CAS:106-51-4; ACS reagent $\geq$ 99%). All chemicals were procured from Sigma Aldrich, Singapore, and were subsequently used without additional purification.

2.2. Fabrication of MIL-100 (Fe)@TiO_2 Composite

Different molar ratios of TiO_2:$Fe(NO_3)_3{\cdot}9H_2O$ were used to synthesize MIL-100 (Fe)@TiO_2 photocatalysts. The $Fe(NO_3)_3{\cdot}9H_2O$ solution concentration and mass of trimesic acid were maintained at 63.31 mmol/L and 1225 mg. The theoretical amount of anatase TiO_2 for different MIL-100 (Fe)@TiO_2 combinations was calculated according to the mole ratio of 3:0.7, 3:1.4, and 3:2.4 ($Fe(NO_3)_3{\cdot}9H_2O$: TiO_2). The as-synthesized photocatalysts were named MxTy, where x and y correspond to the $Fe(NO_3)_3{\cdot}9H_2O$: TiO_2 mole ratio of 3:0.7, 3:1.4, and 3:2.4 (for example, $M_3T_{0.7}$ defines the mole ratio 3:0.7 between $Fe(NO_3)_3{\cdot}9H_2O$ and TiO_2). For the synthesis, 0.05, 0.1, and 0.2 g of anatase TiO_2 were added to 63.31 mmol/L of $Fe(NO_3)_3{\cdot}9H_2O$ solution, followed by mixing and heating at 368.15 K for 120

min. Then, the powders were acquired through multiple washes with DI water and centrifugation for iron residue removal. Subsequently, the powders were re-immersed with 20 mL of DI water and 1.25 g H_3BTC and mixed for 1 h. After 15 min of mixing, the mixture was placed into a Teflon autoclave and heated at 423.15 K for 12 h. The resultant light orange powders were isolated from the autoclave and dispersed in ethanol at 353.15 K for 3 h for H_3BTC residue removal. Eventually, the as-synthesized composite was isolated and dried at 333.15 K overnight. The resulting composite was defined as $M_3T_{0.7}$, $M_3T_{1.4}$, and $M_3T_{2.4}$, respectively.

As the control material, the pristine MIL-100 (Fe) was also fabricated through hydrothermal synthesis as reported elsewhere, with slight modifications (He et al., 2019). Initially, $Fe(NO_3)_3.9H_2O$ and H_3BTC were dissolved in deionized water with additional HNO_3 in the mixture with an overall mole ratio of ($Fe(NO_3)_3 \cdot 9H_2O$:H_3BTC:HNO_3:H_2O = 3.57:2.4:9.02:200). Subsequently, the mixture was magnetically stirred for 1 h, and placed on a Teflon-lined stainless-steel autoclave for isothermal heating at 423.15 K for 12 h. Afterward, the autoclave was naturally cooled to room temperature. Then, the light orange powder was collected through two-step purifications by water and ethanol at 333.15 K for 3 h to remove unreacted reactants. Eventually, the produced pristine MIL-100(Fe) was dried overnight at 373.15 K. The synthesis steps are graphically presented in Figure 1.

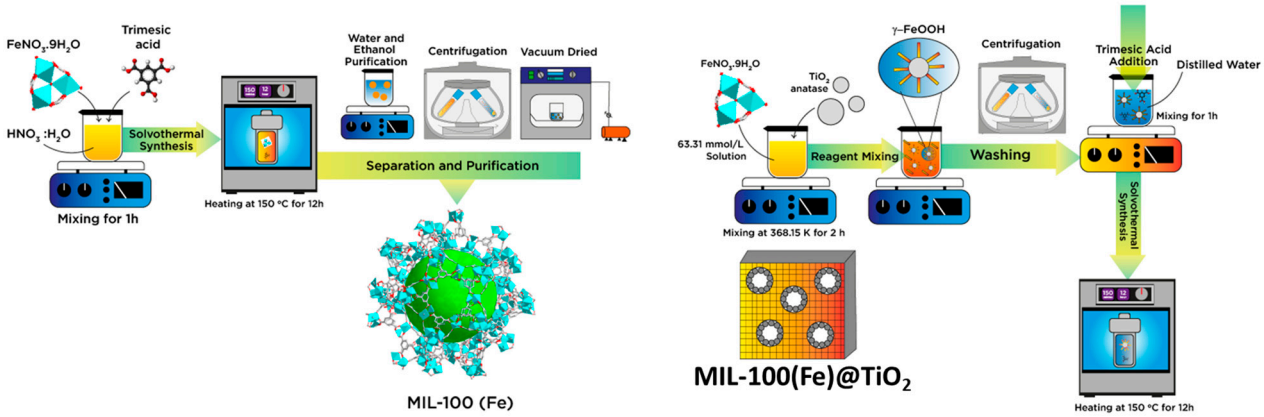

Figure 1. Synthesis Steps of MIL-100(Fe) (**left**) and MxTy Composites (**right**).

2.3. Characterization

The sample phase purity was analyzed through XRD by a Bruker D2 Phaser diffractometer equipped with a Cu Kα radiation source (λ = 0.15406 nm). XRD patterns were measured in the 2θ range of 10–80° with a scan rate of 0.05°/s. The morphological and topological structure of the composite was produced by SEM (JEOL JSM-6500F field emission SEM) at an accelerating voltage of 15.0 kV and a working distance of 9.7 mm. Before the SEM analysis, all solid samples were coated with a thin layer of platinum. The Micromeritics ASAP 2020 analyzer measured N_2 sorption isotherms at 77 K, and the surface area and pore diameter distribution were calculated using Brunauer–Emmett-Teller (BET) and Barrett–Joyner–Halenda (BJH) models. Before the measurements, the samples were initially degassed for 12 h at 200 °C in a vacuum atmosphere. The 209 F3Tarsus measured thermogravimetric analysis (TGA) under air at a heating rate of 10 °C/min up to 600 °C. X-ray photoelectron spectroscopy (XPS) was utilized for chemical state elements of MIL-100 (Fe)@TiO_2 analysis with a VG ESCA Scientific Theta Probe Spectrometer with Al K_α (1486.6 eV) source and 15–400 mm X-ray spot size, operated at 3 KV and 1 mA. The UV diffuse reflectance spectra (DRS) were recorded using a Jasco V-670 UV-visible-near IR spectrophotometer with barium sulfate ($BaSO_4$) as the reflectance standard throughout the 200–800 nm wavelength range. Energy-disperse X-ray spectrometry (EDS) equipped with TEM was used to perform element mapping and atomic composition analysis over the regions of interest. On Bio-Logic Science Instruments with EC-Lab® software, a three-electrode cell with a working electrode, a Pt counter electrode, and a standard Ag/AgCl reference electrode were used to analyze transient photocurrent

density. A solution containing 0.5 mol/L Na_2SO_4 served as the electrolyte. Meanwhile, electrochemical impedance spectra (EIS) were also measured using Bio-Logic Science Instruments with EC-Lab® software. Photoluminescence (PL) spectrum was procured through a Jasco V-670 UV-visible-near IR spectrophotometer (Tokyo, Japan).

2.4. Adsorption and Degradation Photocatalytic Experiments

The current study examined the adsorption/photocatalytic degradation ability of MIL-100 (Fe)@TiO_2 and MIL-100 (Fe) through RhB removability from an aqueous system. The adsorption experiment was carried out in the absence of LED light (50 W; 300–800 nm), whereas photocatalytic degradation was conducted in the presence of an LED lamp. The initial and equilibrium of RB concentrations were analyzed by monitoring the adsorption intensity at λ = 553 nm using a UV-visible spectrophotometer (UV-2550, Shimadzu). The adsorption and photocatalytic degradation studies were performed under several conditions to investigate their important effects during the adsorption/photocatalytic degradation process. Those effects/parameters are as follows:

- Adsorption kinetic study: A series of RhB solutions with an initial concentration of 100 ppm and a volume of 50 mL were prepared. After that, 50 mg of adsorbent was added to each prepared solution. The adsorption was carried out under neutral pH and a shaking water bath at room temperature. The final concentration of RhB was measured at time intervals of 5 min.
- Adsorption isotherm study: A series of RhB solutions with various initial concentrations of 10 to 600 ppm and volumes of 50 mL were prepared. Subsequently, 50 mg of adsorbent was added to each prepared solution. The adsorption was conducted in a shaking water bath at neutral pH and room temperature. The final concentration of RhB was measured after the equilibrium condition was achieved.
- Effect of adsorbent mass: The same procedure as in the kinetic and isotherm studies was employed to study the influence of adsorbent mass on the adsorption of RhB. The various adsorbent mass of 10 to 50 mg was used in this case.
- Effect of MIL-100(Fe) and TiO_2 ratio: In this case, the adsorption procedure was similar to that described above. MIL-100(Fe) with various TiO_2 ratios (3:0.7, 3:1.4, and 3:2.4) were used as the adsorbents.
- Effect of Fenton Addition: A similar adsorption procedure was employed, and before the adsorption took place, 1, 2, or 3 mL of H_2O_2 was added to the mixture.
- Reusability test: Post-adsorption–photocatalytic process, ±0.5 g samples were immersed in 96% ethanol overnight, followed by washing three times until the solutions turned clear. The regenerated samples were used as the adsorbents in the next adsorption–photocatalytic cycle.

The data acquired from the adsorption and photocatalytic degradation experiments were used to investigate the performance of MIL-100(Fe)@TiO_2 towards RhB removal. The specific amount of RhB adsorbed and degraded at equilibrium condition was calculated by Equation (1) as follows:

$$q_e = \frac{(C_0 - C_e)}{m} \times V \quad (1)$$

where q_e is the number of adsorbed RhB at equilibrium (mg/g), C_0 and C_e are the initial and equilibrium concentration (mg/L) of RhB in the aqueous phase, respectively. V is the RhB solution volume (L), and m is the adsorbent dosage (g). The adsorption and degradation efficiency of RhB was measured through the following equation:

$$\eta = \left(1 - \frac{C}{C_0}\right) \times 100\% \quad (2)$$

where C_0 and C represent the initial and equilibrium RhB concentration at a specific time and temperature. For this experiment, all kinetics and isotherms models or equations are listed in Tables 1 and 2.

Table 1. Summary of non-linear kinetic models.

Kinetic Model	Non-Linear Equations	Parameters
Pseudo First Order (PFO)	$Q_t = Q\left(1 - e^{k_1 t}\right)$	Q_t (mg/g): adsorption capacity at various time, t $Q_{e,cal}$ (mg/g): calculated equilibrium capacity of adsorption k_1(1/min): the rate constant of the PFO kinetic model
Pseudo Second Order (PSO)	$Q_t = \frac{Qe^2,cal \ \ k_2 \ t}{1+Q_e,cal \ \ k_2 \ t}$	$Q_{e,cal}$ (mg/g): calculated equilibrium adsorption capacity k_2 (g/mg·min): the rate constant of PSO kinetic model h (mg/g·min)= $Q^2_{e,cal}$ k_2: the initial adsorption rate
Elovich	$Q_t = \frac{\ln(1+(\alpha\beta t))}{\beta}$	α (mg/g·min): the initial adsorption rateβ (g/mg): a parameter related to the activation energy for chemisorption and the extent of surface coverage
Intra-Particle Diffusion (IPD)	$Q_t = k_{IPD}\ t^{0.5}$+C	k_{IPD} (mg/g·min$^{0.5}$): IPD constant rate C (mg/g): a constant that provides value regarding the thickness of the boundary layer.
First Order (FO) Kinetics	$C_t = C_0 \exp(-k_{1p} t)$	C_t (mg/L): final photocatalytic concentration C_0 (mg/L): initial photocatalytic concentration k_{1p} (1/min): the rate constant of FO kinetic model t (min): time of photocatalytic degradation
Second Order (SO) Kinetics	$1 - \frac{C_t}{C_0} = \frac{k_{2p} t}{1+k_{2p} t}$	k_{2p} (L/mg.min): the rate constant of SO kinetic model t (min): time of photocatalytic degradation
Behnajadi, Modirshahla, and Ghanbary (BMG) Models	$1 - \frac{C_t}{C_0} = \frac{t}{m+bt}$	m (min): reciprocal of initial removal rate b (dimensionless): reciprocal theoretical maximum oxidation capacity

Table 2. Summary of non-linear isotherm models.

Isotherm Model	Non-Linear Equations	Technical Constant
Langmuir	$Q_e = \frac{Q_{m,\ \ cal} \ K_L \ C_e}{1+K_L C_e}$	$Q_{m,cal}$ (mg/g): calculated maximum adsorption capacity K_L (L/mg): Langmuir isotherm constant $R_L = [1/(1+ K_L \ C_e)]$; R_L (dimensionless): separation factor
Freundlich	$Q_e = K_F \ C_e^{1/n}$	K_F (mg/g)(L/g)^n: Freundlich isotherm constant related to the adsorption capacity n ($1 < n < 10$): Degree adsorption favorability

Table 2. *Cont.*

Isotherm Model	Non-Linear Equations	Technical Constant
Redlich-Peterson (R-P)	$Q_e = \frac{K_{RP}\ C_e}{1+\alpha_{RP}\ C_e{}^{g}}$	K_{RP} (L/g): Redlich–Peterson isotherm constant α_{RP} (L/mg): Redlich–Peterson isotherm constant g ($0 < g < 1$): Redlich–Peterson isotherm binding constant
Sips	$Q_e = \frac{q_{ns} K_s\ C_e{}^{n_s}}{1+K_s\ C_e{}^{n_s}}$	K_S (L/g): Sips isotherm model constant q_{ns} (mg/g): Sips isotherm maximum adsorption capacity n_S: Sips isotherm model exponent
Toth	$Q_e = \frac{Q_{m,\ To}\ C_e}{(K_{To}+C_e{}^{n_{To}})^{1/n_{To}}}$	$Q_{m,To}$ (mg/g): maximum adsorption capacity K_{To} (mg/L): Toth isotherm constant n_{To}: Toth isotherm model exponent; $0 < n_{To} \leq 1$
Temkin	$Q_e = \frac{RT}{b_T} ln\ K_T\ C_e$	b_T (J/mol): Temkin isotherm binding constant K_T (L/g): Temkin isotherm equilibrium binding constant R (8.314 J/mol.K): the ideal gas constant

3. Results and Discussion

3.1. Characterization

The crystallinity and phase purity of the obtained M_xT_y and TiO_2 (anatase) were measured using X-ray diffraction (XRD) (Figure 2). According to the XRD diffractograms, each synthesized M_xT_y resembled pristine MIL-100(Fe) peaks at 2θ angles of 11° and 20°, excluding $M_3T_{0.7}$. This resemblance also corresponded to the theoretical MIL-100(Fe) single-crystal XRD pattern based on CCDC 640,536 [12]. Other than MIL-100(Fe) peaks, the obtained M_xT_y also exhibited some key TiO_2 anatase peaks at 2θ angles of 28°, 36°, 56°, and 70°. These peaks corresponded to the (101), (211), and (204) crystal planes of TiO_2 (anatase) and fit the TiO_2 (anatase) simulated card (ICSD-50447) [13]. However, there was a slight shift within the observed peaks on the composite, compared with its pristine component. This can result from the increasing or decreasing band gaps, which is possible when two materials are combined. We can still safely assume that the peak shown on the composite was the peak of the pristine component because the shifting was consistent within each peak. With these two indicators present in the obtained M_xT_y, the XRD pattern provided sufficient evidence of TiO_2 characteristic peaks in the M_xT_y crystalline.

Furthermore, the SEM images were implemented further to clarify the structures and morphologies of the synthesized M_xTy. As shown in Figure 3, the synthesized M_xTy had an irregular triangle shape with a size in the range of nanoporous materials. According to SEM images, the synthesized particles tended to agglomerate and create an aggregate of materials, affecting the adsorption and photocatalytic degradation performance. In addition, energy-dispersive X-ray spectroscopy (EDXS) was also employed to confirm the existence and distribution of each precursor inside the synthesized M_xTy. The distribution of precursors inside the synthesized MxTy showed a match between the expected and actual metal ratios to TiO_2 (Figure 4).

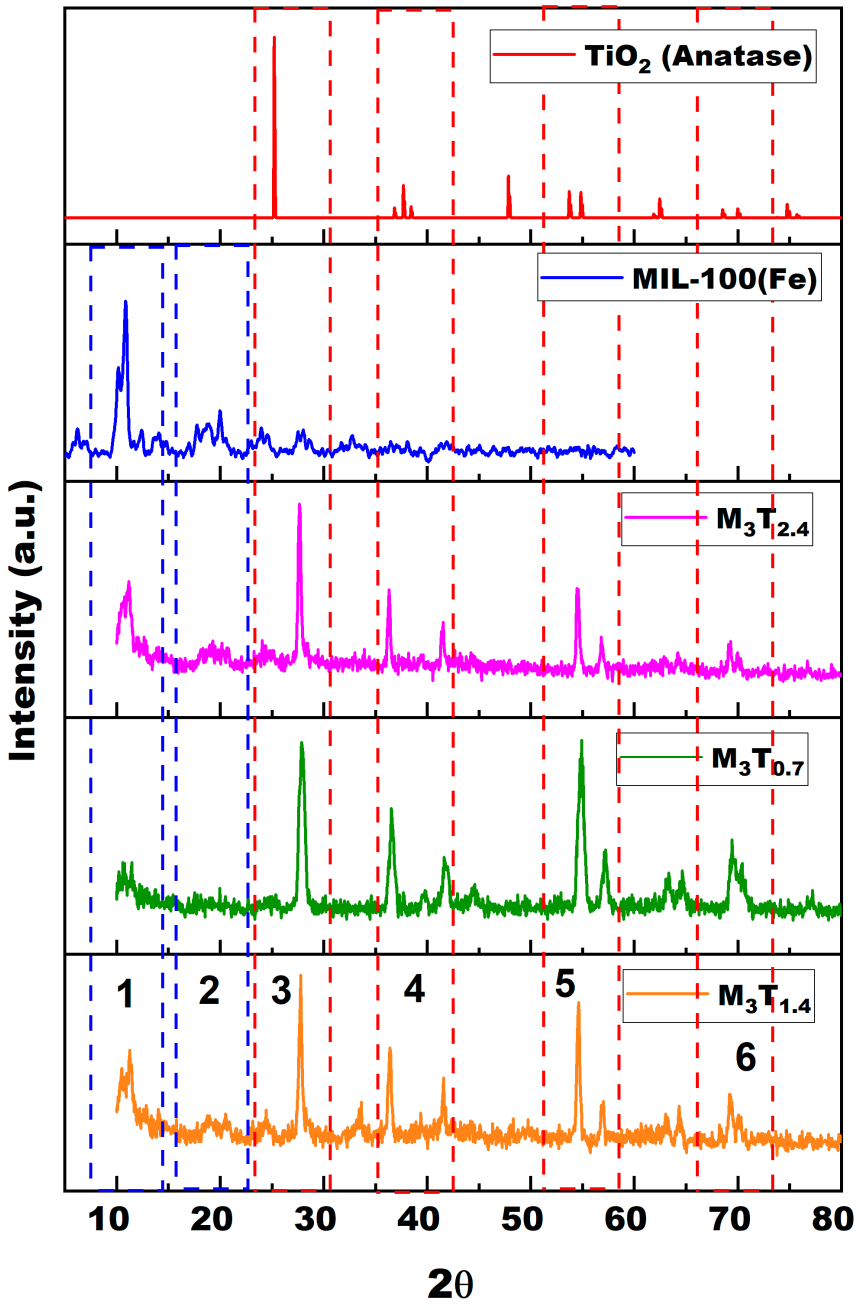

Figure 2. XRD patterns of pristine TiO_2, MIL-100(Fe), and M_xT_y composites.

To further clarify the presence of each pristine MIL-100(Fe) and TiO_2 anatase inside the composite, the thermogravimetric analysis (TGA) was conducted, and is shown in Figure 5A. A weight loss around 200 °C was assigned to the removal of water molecules plus the desorption of ligand from the surfaces of the nanocrystals [10]. The decomposition of carboxylic acid was observed between 245–450 °C, which corresponded to the composite framework's collapse. When heated further, well over 450 °C, the TiO_2 anatase exhibited great thermal stability. In the $M_3T_{1.4}$ curve, we can see that the graph is more stable at high temperatures than pristine MIL-100(Fe), which indicates that the stability must come from the TiO_2 anatase presence within the $M_3T_{1.4}$. To study the pore structure of the synthesized materials, nitrogen sorption analysis was conducted, and is shown in Figure 5B. From the N_2 sorption result shown in Figure 5B, the TiO_2 anatase exhibited type II isotherm, and the composite isotherm exhibited type I and IV isotherm. The surface pore area was calculated, and is shown in Table 3. According to those results, the optimum ratio for MIL-100(Fe) and

TiO_2 to create the most significant surface area, which will benefit the application towards adsorption and photocatalytic degradation, was $M_3T_{1.4}$.

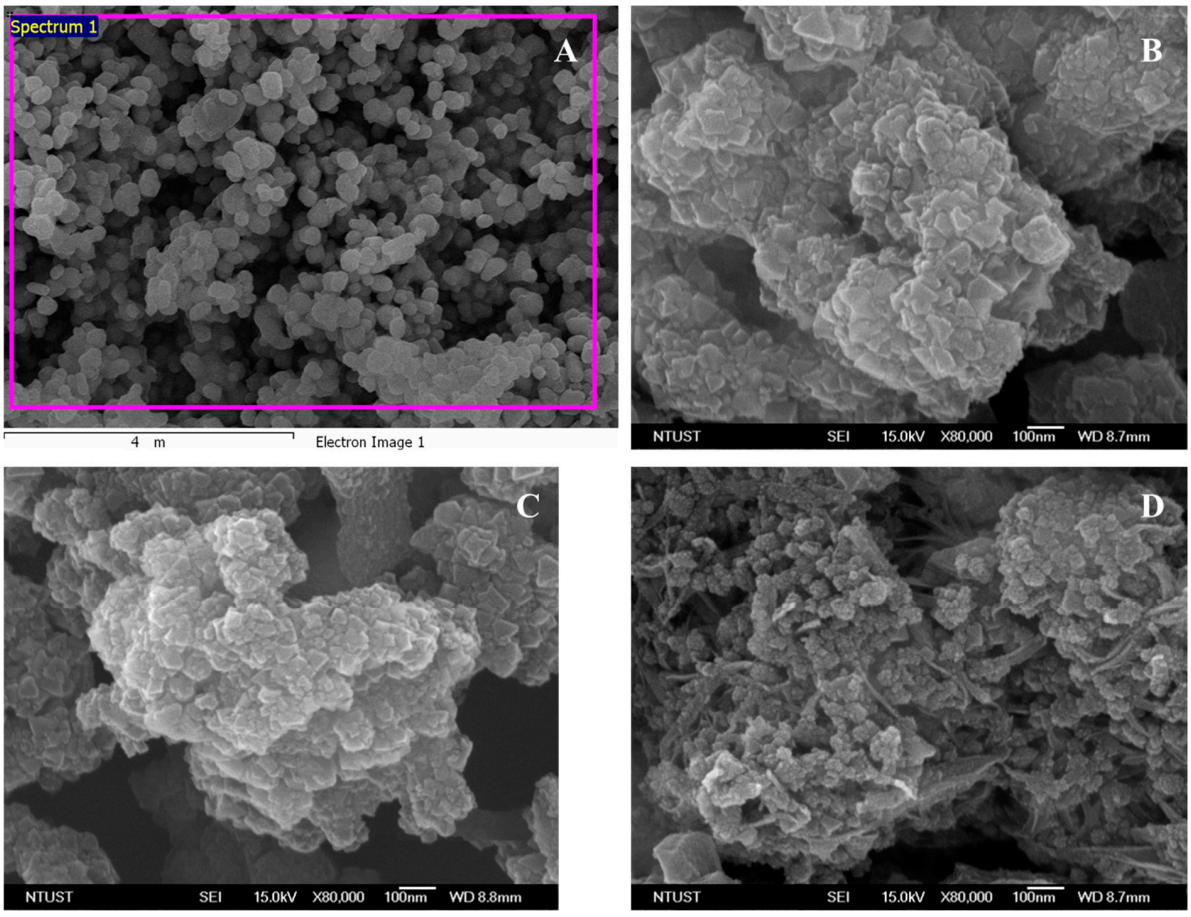

Figure 3. SEM images of (**A**) TiO_2 anatase; (**B**) $M_3T_{0.7}$; (**C**) $M_3T_{1.4}$; (**D**) $M_3T_{2.4}$.

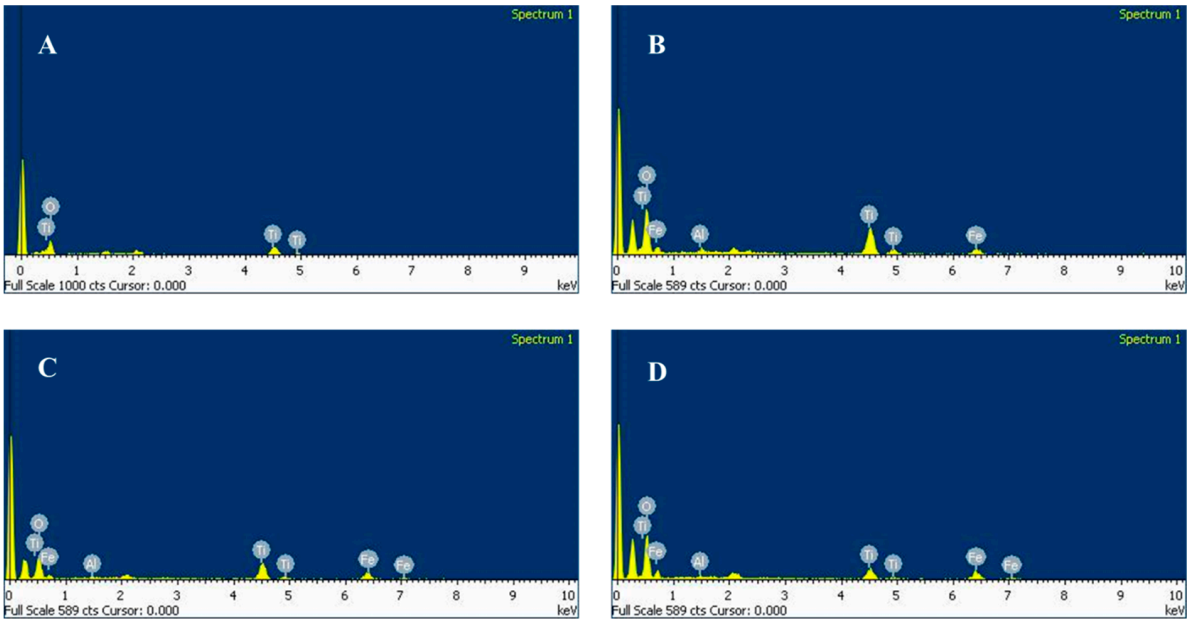

Figure 4. EDXS pattern of: (**A**) TiO_2 anatase; (**B**) $M_3T_{0.7}$; (**C**) $M_3T_{1.4}$; (**D**) $M_3T_{2.4}$.

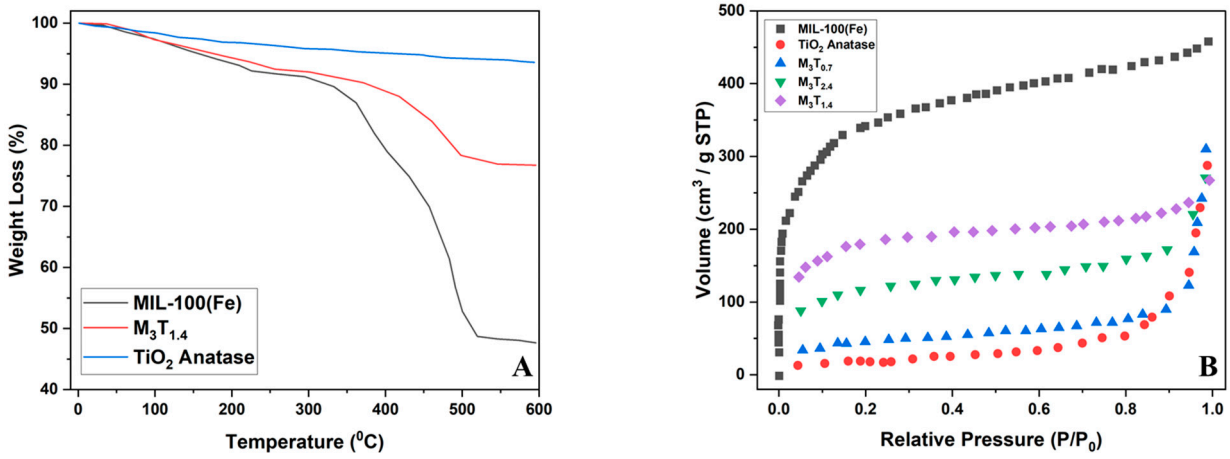

Figure 5. (**A**) TGA Curve and; (**B**) N_2 sorption isotherm.

Table 3. BET surface area results.

Materials	BET Surface (m^2/g)
MIL-100(Fe)	1576.4
$M_3T_{0.7}$	179.2
$M_3T_{1.4}$	450.7
$M_3T_{2.4}$	799.5
TiO_2 anatase	79.3

The photoluminescence spectra (PL) for each M_xT_y were investigated from 300 nm to 800 nm (Figure 6). Guo et al. [14] reported that the lower the PL intensity obtained, the more efficient the transfer of the photoinduced carriers and their generation inside the whole system. Distinctly, $M_3T_{1.4}$ showed the lowest PL curve, with $M_3T_{2.4}$ showing the highest PL curve. This phenomenon shows that $M_3T_{1.4}$ provided significantly enhanced separation efficiency and reduced recombination rate of the excited electron-hole pairs, the most suitable/profitable to use in the photocatalytic degradation system.

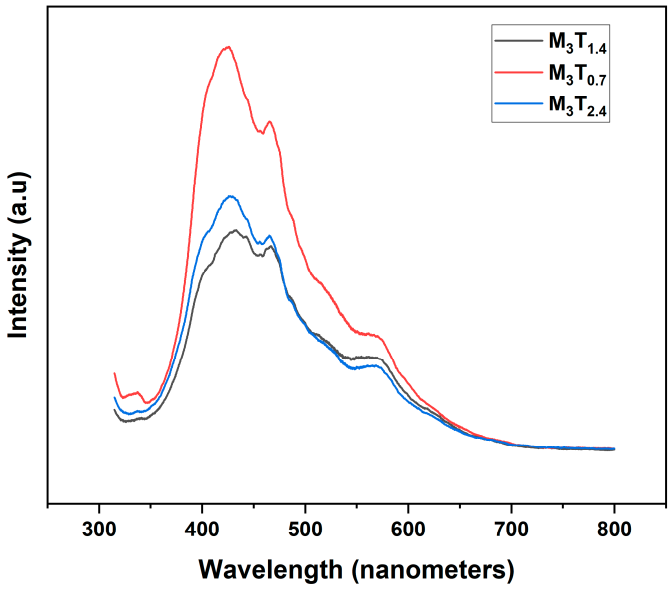

Figure 6. PL spectra of M_xT_y composites.

The stability of the synthesized M_xT_y under visible light irradiation was studied using the transient photocurrent tests. The experiments were recorded under visible light irradiation, which was switched on and off regularly. As shown in Figure 7, the photoexcited electrons that produced the photocurrent were observed when the light was turned on. The photo-generated carriers' better separation efficiencies and a longer lifetime is indicated by higher photocurrent density [14]. $M_3T_{1.4}$ exhibited higher photocurrent density than other ratios, indicating that $M_3T_{1.4}$ can provide good separation efficiencies and a longer photo-generated carrier's lifetime than other synthesized ratios.

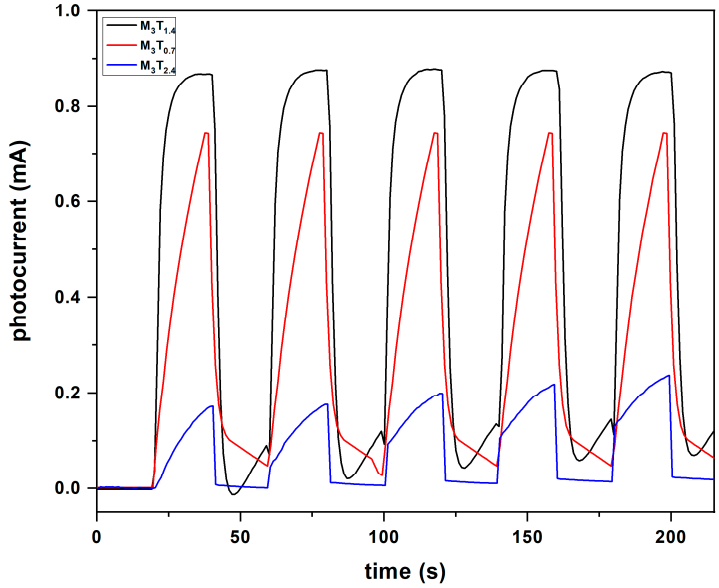

Figure 7. Transient photocurrent density spectra of M_xT_y composites.

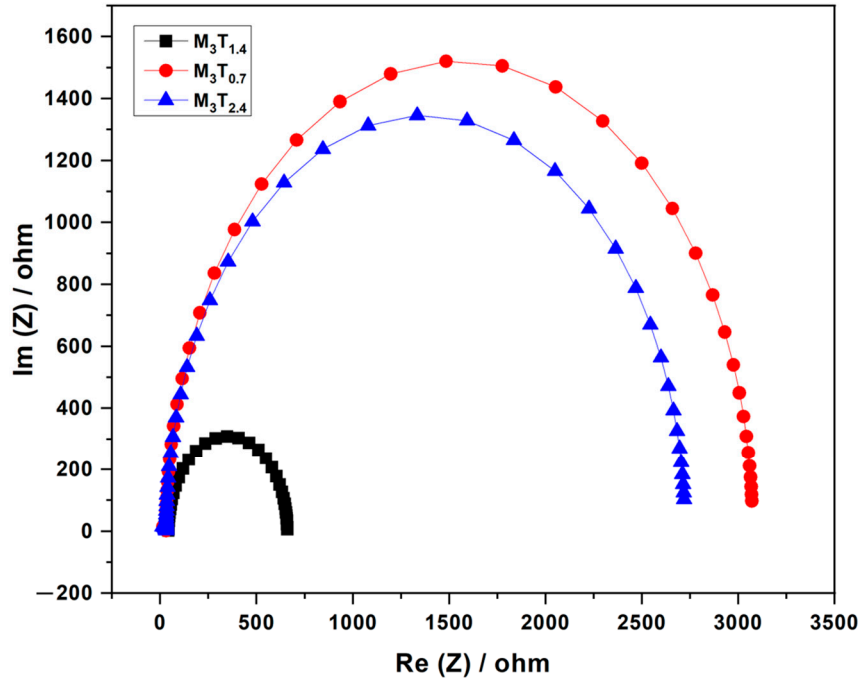

Figure 8. EIS spectra of M_xT_y composites.

The impedance of the photoanodes was used to examine the charge transport capability, and electron impedance spectra (EIS) tests were conducted. A smaller arc diameter at high frequency implies high efficient charge separation and electron transfer [14]. As shown in Figure 8, $M_3T_{1.4}$ also exhibited a smaller arc diameter than other M_xT_y, indicating efficient charge separation and electron transfer capability of the material compared with other M_xT_y. The EIS results were consistent with the PL and transient photocurrent tests, indicating the highest photocatalytic capability efficiency of the $M_3T_{1.4}$ under visible light irradiation.

The chemical bonding of MIL-100(Fe) and TiO_2 atoms was characterized using XPS (Figure 9). The full survey spectrum of XPS distinctly disclosed the existence of Fe, O, Ti, and C elements. The high-resolution spectra of O1s, Ti2p, and Fe2p are also shown in Figure 8. In the spectrum of O1s, peaks at 528.6, 530.3, and 531.7 eV were assigned to C=O bonding (carboxyl group in benzene tricarboxylic acid), O-Fe bond (ligand bonding with the metal), and Ti-O-Ti bond (from TiO_2 molecules) [10]. Peaks at 458.6 and 466.3 eV in the spectrum of Ti2p corresponded to Ti $2p_{3/2}$ and Ti $2p_{1/2,}$ respectively. The binding energy difference of 7.7 eV between Ti $2p_{3/2}$ and Ti $2p_{1/2}$ showed the chemical state of Ti^{4+} in MIL-100(Fe)@TiO_2 materials [15]. In the Fe2p spectrum, two peaks were observed at 712.9 and 727.3 eV, which were assigned to Fe $2p_{3/2}$ and Fe $2p_{1/2.}$ Therefore, the chemical state of Fe(III) was present in MIL-100(Fe) [16]. Peaks at 284.6 eV and 288.9 eV in the spectrum of C1s corresponded to the benzene ring (from the benzene tricarboxylic acid) and a carboxyl group. XPS analysis provided sufficient evidence for the chemical interaction between MIL-100(Fe)@TiO_2 molecules.

The optical absorption capability of synthesized M_xT_y was investigated using UV-Vis DRS. As seen in Figure 10, $M_3T_{1.4}$ exhibited a higher and broader spectrum than other M_xT_y, indicating that $M_3T_{1.4}$ can be considered an optimum metal-to-TiO_2 ratio for its ability to absorb lightwaves. The optical band gap of each M_xT_y was calculated using the Kubelka–Munk function versus the energy of absorbed light [17]. Figure 10 shows that the optical band gap of $M_3T_{1.4}$ was around 3.26 eV, $M_3T_{0.7}$ was around 3.67 eV, and $M_3T_{2.4}$ was around 4.16 eV. Figure 11 shows the Tauc plot obtained from UV-Vis DRS spectra of each precursor, as well each synthesized ratio.

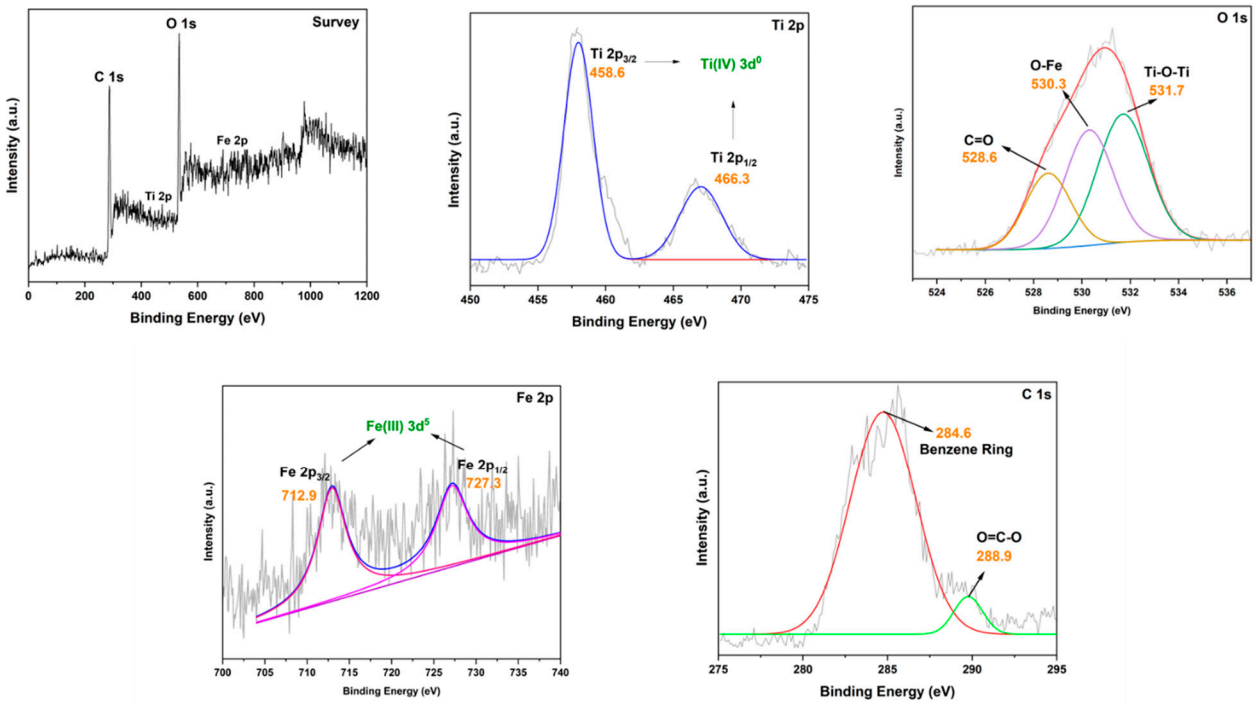

Figure 9. XPS spectra of M_xT_y.

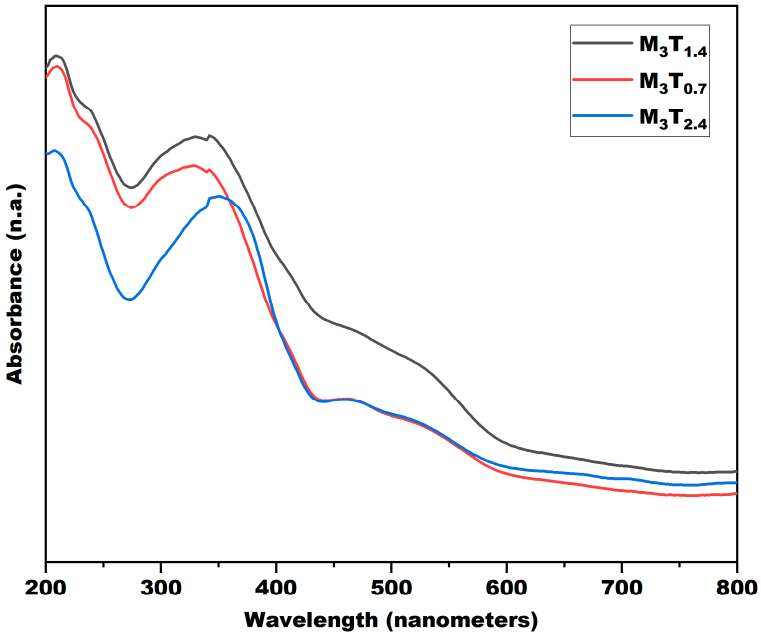

Figure 10. UV-Vis DRS spectra of M_xT_y composites.

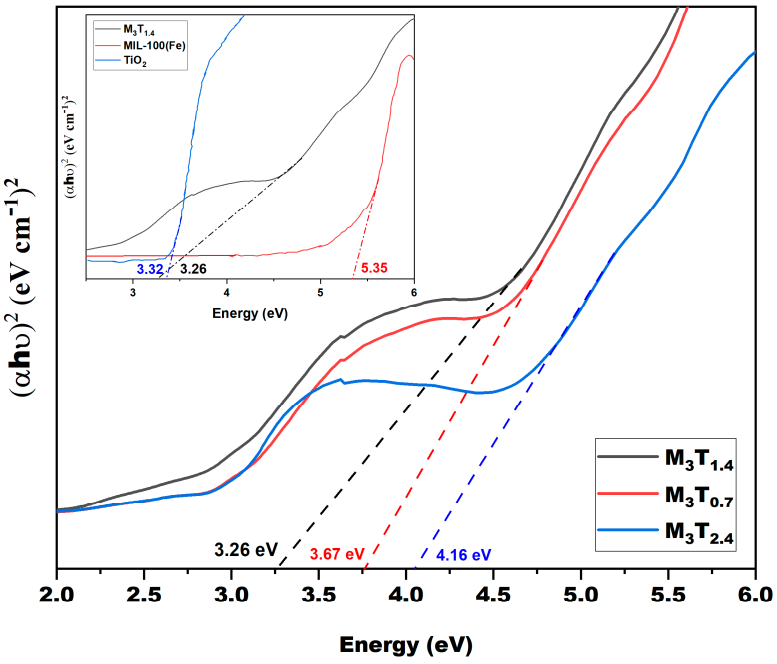

Figure 11. Tauc plot of UV-Vis DRS spectra composites.

The photocatalytic capability of composite materials was also compared with its precursors. The individual band gap of $M_3T_{1.4}$, which is gained from UV-Vis DRS, combined with the geometric mean of Mulliken electronegativity values of its constituent atoms, was used to calculate the conduction and valence band of materials using this empirical formula [13]:

$$E_{VB} = X - E_e + 0.5E_g \quad (3)$$

$$E_{CB} = E_{VB} - E_g \quad (4)$$

where variable "X" represents the Mulliken electronegativity of an element (5.81 eV for TiO_2, 6.74 eV for MIL-100(Fe), and 6.69 eV for MIL-100(Fe)@TiO_2), E_e is the energy of free electrons on the hydrogen scale with a value constant of 4.5 eV vs. NHE [18], and E_g

represents the sample's bandgap energy measured using UV-Vis DRS. Table 4 summarizes the values for E_g, E_{CB}, X, and E_{VB} of the composites and their precursors.

Table 4. Summary of electronegativity, X, band gap energy E_g (in eV), energy positions of band edges E_{CB} and E_{VB} (in eV) of composite and its precursors.

Materials	X (eV)	E_G (eV)	E_{CB} (eV)	E_{VB} (eV)
MIL-100(Fe)	6.74	5.35	−0.43	4.91
TiO_2 anatase	5.81	3.32	−0.35	2.97
MIL-100(Fe)@TiO_2 ($M_3T_{1.4}$)	6.69	3.26	0.61	3.87

3.2. Adsorption Kinetics and Isotherm

Rhodamine B's (RhB) adsorption kinetics onto M_xT_y were correlated using pseudo-first, pseudo-second, and Elovich models, while the Langmuir, Freundlich, Temkin, Sips, Toth, and Redlich–Peterson adsorption equations were used to represent the experimental adsorption data. The fitted pseudo-first kinetic models for $M_3T_{0.7}$, $M_3T_{1.4}$, and $M_3T_{2.4}$ are shown in Figure 12A, while the fitted pseudo-second and Elovich models for $M_3T_{1.4}$ are shown in Figure 12B. Based on the non-linear kinetic correlation shown in Table 5, pseudo-first-order kinetics represented the experimental data better than other kinetics equations. Figure 12A shows that the system reached equilibrium in approximately 60 min. Figure 12C shows the intra-particle diffusion model for studying the diffusion mechanism and its rate towards the RhB adsorption process. The non-linear curve between q_e and $t^{0.5}$ indicates that the adsorption occurred in multiple steps. The first stage involved the fast transfer from the solution to the surface of M_xT_y, which utilized previous isotherm models, driven by the electrostatic interactions (physical sorption) between the organic dyes and water molecules. The next step was a slower diffusion from the surface into the pore of the MxTy nanoparticles, which corresponded to the final equilibrium state of the adsorbate and adsorbent. The experimental adsorption isotherm data and fitting for Langmuir models towards pristine MIL-100(Fe), $M_3T_{0.7}$, $M_3T_{1.4}$, and $M_3T_{2.4}$ are shown in Figure 13A, while the other fitted isotherm models for $M_3T_{1.4}$ are shown in Figure 13B. Based on the non-linear isotherm correlation shown in Table 6, the Langmuir model isotherm represented the experimental data better than other isotherm equations, indicated by a higher correlation coefficient (R^2). It can also be seen that $M_3T_{1.4}$ indicated the highest equilibrium adsorption capacity (q_e), compared with other composites.

According to Giles et al. [19], the classification of the isotherm plots in all experiments represents the L-curve (normal or Langmuir isotherm) with subclass 2. The L-curve frequently demonstrated the behavior of solute adsorption in an aqueous solution onto an adsorbent. In most Langmuir isotherm cases, the solute adsorption continuously increased along with the solute concentration and adsorption site availability, until the active sites reached their saturation capacity. This statement infers that the availability of the active site plays a significant role in determining the adsorbent's adsorption capacity. Therefore, it was rational for MIL-100 (Fe)@TiO_2 with the optimum mole ratio of 3:1.4 to have high adsorption capacity since it provided better adsorption accessibility of solute towards active sites (Table 3). In addition, the refinement of adsorption sites available through the structural porosity adjustment led to a rise in the affinity constant or Langmuir constant (K_L). This suggests that a strong affinity occurred between adsorbate and adsorbent [20]. Meanwhile, the plateau plots with subclass 2 were observed after a specific adsorption time. This phenomenon was caused by the adsorbent's monolayer saturation, resulting in the solute affinity towards the adsorption sites being lower than the solvent. In this case, increasing adsorption temperature negatively influenced the attachment of solute towards new sites after reaching its first saturation capacity. The increasing temperature decreased the adsorption capacity of M_XT_Y (Figure 13C). As the temperature rose, the nature of the solute dye molecules' solubility increased, which further assisted the mobility and diffusion of RhB leaving the adsorption sites. This theory was consistent with the

adsorption data of RhB onto MIL-100 (Fe)@TiO_2, where the maximum saturation capacity (q_{max}) decreased along with the increase in temperature (Table 7), which indicated the adsorption was exothermic. t

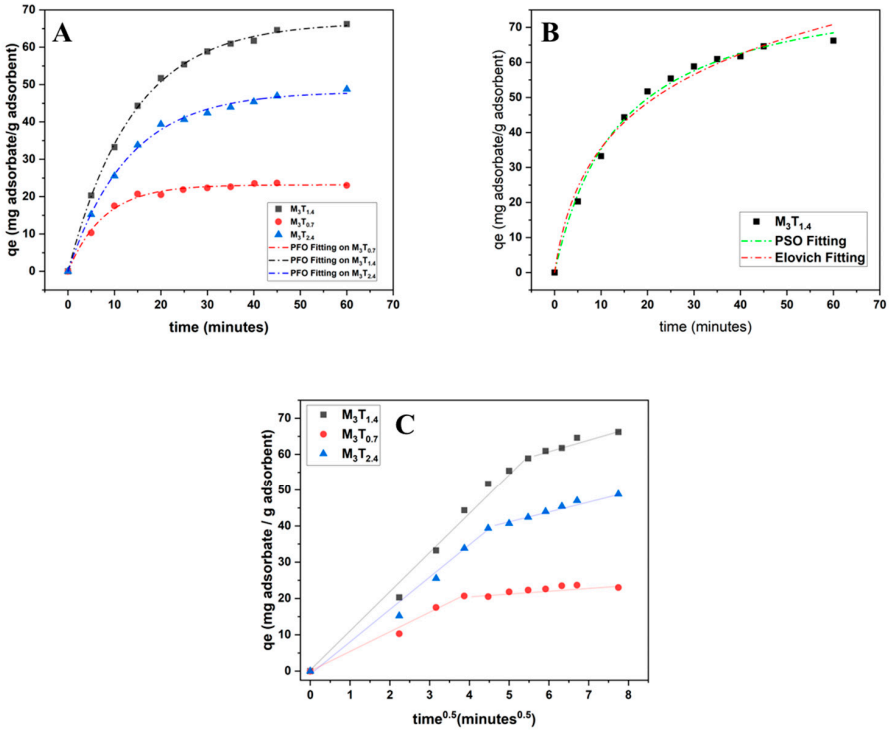

Figure 12. Adsorption kinetics models (**A**) each component towards PFO equation; (**B**) $M_3T_{1.4}$ towards other kinetic models; (**C**) intra-particle diffusion models.

3.3. Thermodynamic Study

The thermodynamic system fundamentally evaluated the adsorption system to determine physisorption or chemisorption. Physisorption (known as physical adsorption) is controlled by relatively weak coordination through van der Waals forces, while chemisorption (or chemical adsorption) takes advantage of the sharing electron's ability of adsorbent and adsorbate to construct strong chemical bonding. Judging by the value of several thermodynamic parameters, such as the Gibbs energy change (ΔG°) and the enthalpy change (ΔH°), both physical and chemical adsorption can be evaluated. The thermodynamic parameters also determined the system behavior during the adsorption. For instance, the spontaneity of the system was determined based on the value of ΔG° (the adsorption process will not be favorable and non-spontaneous when the ΔG° exhibits a positive quantity, while it will be feasible and spontaneous with the negative value of ΔG°). Meanwhile, the value of ΔH° reflects whether the system is exothermic ($\Delta H^\circ < 0$) or endothermic ($\Delta H^\circ > 0$). The chemical adsorption was dominantly presented by the system with endothermic nature, which required a certain amount of energy from the surroundings to construct interaction. By contrast, the exothermicity system was indicated by the decrease in adsorption capacity with the increasing temperature; the system releases heat energy toward the surroundings. The ΔS° value also draws a significant aspect in determining the adsorbate distribution pattern at the solid/solution interface, whether it is less than zero ($\Delta S^\circ < 0$) or more randomly distributed ($\Delta S^\circ > 0$). In addition, the positive and negative values of ΔS° also correspond to adsorption's dissociative and associative mechanism.

Table 5. Parameters of kinetic models.

Adsorbents	Model	Parameters *		
		R^2	k_1	$Q_{e,cal}$
MIL-100(Fe)	PFO	0.9967	0.0769	58.3991
$M_3T_{0.7}$		0.9934	0.1297	23.1596
$M_3T_{1.4}$		0.9992	0.0717	66.6876
$M_3T_{2.4}$		0.9971	0.0775	48.1273
		R^2	k_{IPD}	C
MIL-100(Fe)	IPD	0.9844 0.9825	10.7556 3.8083	1.9822 30.5665
$M_3T_{0.7}$		0.9712 0.9559	4.9588 1.3586	0.1858 14.746
$M_3T_{1.4}$		0.9894 0.9005	11.3210 2.9697	1.4738 43.558
$M_3T_{2.4}$		0.9805 0.9404	8.5686 3.6735	1.2118 21.778
		R^2	$k_2 \times 10^4$	$Q_{e,cal}$
MIL-100(Fe)	PSO	0.9945	11.0122	73.0601
$M_3T_{0.7}$		0.9839	63.2139	26.7105
$M_3T_{1.4}$		0.9952	8.5068	84.3482
$M_3T_{2.4}$		0.9942	13.3000	60.1353
		R^2	α	β
MIL-100(Fe)	Elovich	0.9837	8.8664	0.0543
$M_3T_{0.7}$		0.9599	13.1702	0.2003
$M_3T_{1.4}$		0.9843	8.9117	0.0457
$M_3T_{2.4}$		0.9828	7.4064	0.0662

* Calculated based on non-linear fitting on Origin Pro 2021 Software (Northampton, MA, USA).

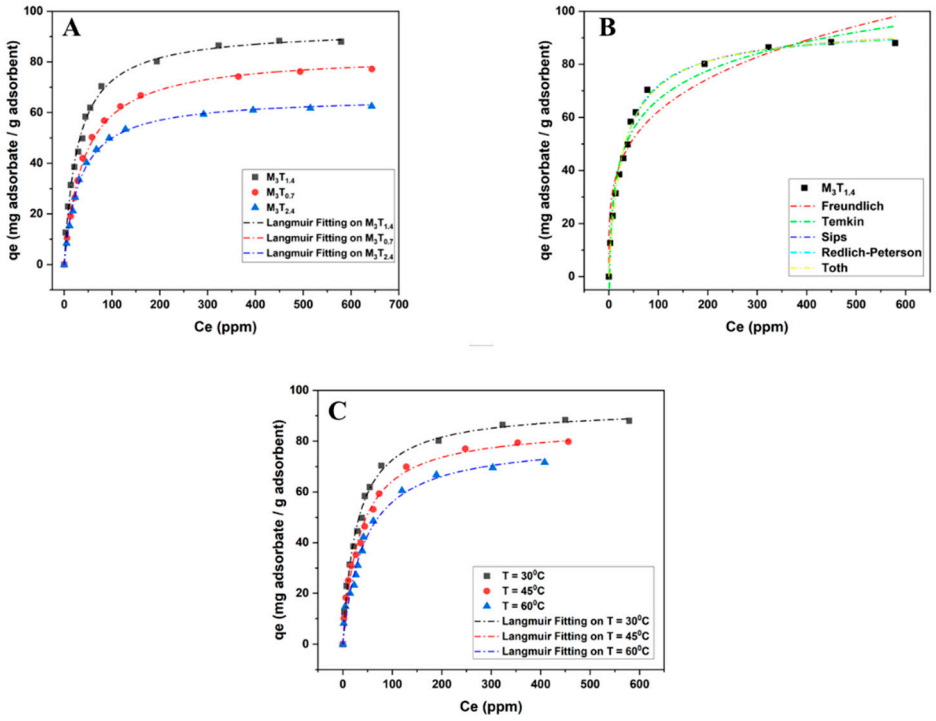

Figure 13. Adsorption isotherm models: (**A**) each component towards the Langmuir model; (**B**) $M_3T_{1.4}$ towards other isotherm models; (**C**) at different temperatures.

Table 6. Parameters of isotherm equations.

Adsorbents	Model	Parameters *			
		R^2	K_L	$Q_{max\ (calc)}$	
MIL-100(Fe)	Langmuir	0.9977	0.0344	58.9810	
$M_3T_{1.4}$		0.9944	0.0354	93.0977	
$M_3T_{0.7}$		0.9975	0.0243	83.1217	
$M_3T_{2.4}$		0.9977	0.0306	66.2711	
	Freundlich	R^2	K_F	n	
MIL-100(Fe)		0.9322	10.5269	3.5129	
$M_3T_{1.4}$		0.9282	18.9381	3.8696	
$M_3T_{0.7}$		0.9158	13.7269	3.5249	
$M_3T_{2.4}$		0.9118	12.6302	3.7898	
	R-P	R^2	K_{RP}	α_{RP}	g
MIL-100(Fe)		0.9968	2.0290	0.0349	0.9932
$M_3T_{1.4}$		0.9946	3.4787	0.0415	0.9827
$M_3T_{0.7}$		0.9975	2.0290	0.0349	0.9999
$M_3T_{2.4}$		0.9971	2.0155	0.0300	0.9939
	Sips	R^2	K_S	q_{ns}	n_s
MIL-100(Fe)		0.9988	0.0410	58.9019	0.9755
$M_3T_{1.4}$		0.9947	0.0464	95.9308	0.9004
$M_3T_{0.7}$		0.9999	0.0161	80.0316	1.1376
$M_3T_{2.4}$		0.9982	0.0392	63.8829	0.9181
	Toth	R^2	$Q_{m,To}$	K_{To}	n_{To}
MIL-100(Fe)		0.9973	58.2251	29.0698	0.9883
$M_3T_{1.4}$		0.9950	96.1932	15.9191	0.8679
$M_3T_{0.7}$		0.9975	83.1153	41.2046	0.9921
$M_3T_{2.4}$		0.9977	66.2678	32.6964	0.9993
	Temkin	R^2	b_T	K_T	
MIL-100(Fe)		0.9874	239.5997	0.5517	
$M_3T_{1.4}$		0.9789	159.7044	0.6830	
$M_3T_{0.7}$		0.9758	161.7385	0.3309	
$M_3T_{2.4}$		0.9719	211.4439	0.4610	

* Calculated based on non-linear fitting on Origin Pro 2021 Software (Northampton, Massachusetts, USA).

Table 7. Parameters of Langmuir equation at various temperatures.

T(K)	R^2	K_L	ρ (g/L)	$Q_{max\ (calc)}$
303.15	0.9944	0.0354	996.584	93.0977
318.15	0.9874	0.0293	991.003	86.1641
333.15	0.9837	0.0226	985.917	80.7086

The conventional way to determine the thermodynamic parameters of adsorption is based on the third principle of thermodynamic laws:

$$\Delta G^o = -RTln\ (K_c) \quad (5)$$

The correlation between ΔG°, ΔH°, and ΔS° can be written as follows:

$$\Delta G^{o} = \Delta H^{o} - T\Delta S^{o} \quad (6)$$

Substitution of Equation (5) into Equation (6) produces a well-known van 't Hoff equation which is widely used to obtain the thermodynamics parameters of adsorption:

$$\ln(K_c) = -\frac{\Delta H^{o}}{RT} + \frac{\Delta S^{o}}{R} \quad (7)$$

The calculation or determination of the thermodynamic equilibrium constant, K_c, is still under debate [21]. Various approaches have been proposed for that purpose; several directly use the parameters obtained from the fitting of the experimental adsorption data using adsorption isotherm equations as the equilibrium constant [22]. This approach neglects the dimensionality of K_c since the adsorption isotherm parameters usually have their units. Various researchers also developed or used other thermodynamic approaches that neglect the dimensionality of K_c to calculate the adsorption thermodynamics [23].

Several issues that need to be considered in determining the valid K_c and accurate thermodynamic parameters are:

- The thermodynamic equilibrium constant, K_c, should be dimensionless;
- The selection of adsorbate concentration is critical to determine which model could be used;
- The regression coefficient (R^2) of the van 't Hoff equation must be high and linear, and calculated based on temperature with kelvin units (K);
- The behavior of isotherms, experimental data, and thermodynamic parameters should be logical and consistent.

In recent studies, there have been two primary approaches to determining the thermodynamic equilibrium constant: (1) the distribution or partition coefficient model; (2) the isotherm adsorption model constant (the most common Langmuir constant). This study employed the partition coefficient model as the starting point for model development.

The partition model, which observes the adsorption system as the apportionment of adsorbate between solid and liquid phases, is an old-fashioned model for liquid-phase adsorption. Biggar and Cheung [24] proposed this model to evaluate the thermodynamic adsorption of picloram onto several soils. For this typical adsorption system, the chemical equation has been described as follows:

$$A \quad \leftrightarrow \quad A_{(s)} \quad (8)$$

where $A_{(s)}$ is the adsorbate in the solid phase, while $A_{(l)}$ is the adsorbate in the liquid phase. The equilibrium parameter of Equation (8) can be written as follows:

$$K_p = \frac{\left[A_{(s)}\right]}{\left[A_{(l)}\right]} = \frac{C_s\,\gamma_s}{C_e\,\gamma_e} \quad (9)$$

where $[A_{(s)}]$ and $[A_{(l)}]$ are the activity of adsorbate in adsorbent and solution at equilibrium, respectively. Meanwhile, γ_s and γ_e are the activity coefficient of adsorbate on the adsorbent and in solution during equilibrium. C_s (mg/L) and C_e (mg/L) correspond to the adsorbate concentration on the adsorbent and in solution at equilibrium. In specific conditions, the value of the activity coefficient reached unity when nearly zero adsorbate concentration was observed, and Equation (9) becomes:

$$\lim_{C_s=0} \frac{C_s}{C_e} = \frac{a_s}{a_e} = K_p \quad (10)$$

In this model, the K_p value can be acquired by plotting ln (C_s/C_e) (y-axis) vs. C_s (x-axis) and extending the C_s value to zero, and the intersection with the vertical axis produces the value of K_p. The high value of the regression coefficient (R^2) should be obtained to obtain the valid value of K_P.

Khan and Singh proposed the distribution coefficient (K_d) based on the partition model [25]. The distribution coefficient can be written as follows:

$$K_d = \frac{Q_e}{C_e} \tag{11}$$

Q_e (mg/g) is the amount of adsorbate in the solid at equilibrium condition, while the symbol C_e (mg/L) represents the equilibrium concentration. This method obtains the K_d value similarly to Equation (10). As the distribution coefficient, K_d calculated from Equation (11) has a unit of L/mg. Furthermore, in an adsorption system, each value of Q_e corresponds to a value of C_e. At the high-medium to high value of C_e, in most adsorption systems, the value of Q_e does not increase linearly, and it becomes constant when a saturated condition is achieved. The inclusion of adsorption isotherm at medium and high equilibrium concentrations always results in a low value of the regression coefficient (R^2).

To obtain the value of K_d with a high R^2, the value of Q_e should be linearly increased with C_e, and this condition can be achieved when the adsorption isotherm is linear. The linear part of the adsorption isotherm occurs when the equilibrium concentration is low or very low. Now consider the Langmuir equation as follows:

$$Q_e = Q_{max}\frac{K_L C_e}{1 + K_L C_e} \tag{12}$$

where Q_{max} (mg/g) is Langmuir's parameter representing the adsorbate's adsorption capacity, and K_L (L/mg) is the adsorption affinity. At very low equilibrium concentration (C_e << 1), the Langmuir equation can be written as:

$$Q_e = Q_{max}.K_L.C_e \tag{13}$$

Equation (13) gives a linear correlation between Q_e and C_e, and:

$$\frac{Q_e}{C_e} = Q_{max}K_L \tag{14}$$

Substitution of Equation (14) to Equation (11) gives:

$$K_d = Q_{max}.K_L \tag{15}$$

Here the unit of K_d obtained from Equation (15) is L/g. Several studies directly used the value of K_d as the equilibrium constant K_c (dimensionless constant) to obtain thermodynamic parameters of several adsorption systems. Since the unit L in K_d is the unit volume of solution, it can be easily converted into mass by multiplying with the density of solution ρ (g/L)

$$K_d = Q_{max}.K_L.\rho \tag{16}$$

The distribution coefficient calculated from Equation (16) is dimensionless. Equation (16), for the first time, was proposed by Milonjić [26] by taking the density of water to 1000.

$$K_d = Q_{max}.K_L.1000 \tag{17}$$

The thermodynamics properties of RhB adsorption onto the surface of MIL-100(Fe)@TiO_2 are given in Table 8. At all temperatures examined, the Gibbs free energy (ΔG°) for the adsorption of RhB was negative with a value lower than −20 kJ/mol, which indicated the spontaneous nature of RhB adsorption towards MIL-100(Fe)@TiO_2 and that physisorption controls the mechanism. Increasing temperature decreased the ΔG° value, implying that the

affinity of RhB onto MIL-100 (Fe)@TiO_2 was diminished at higher temperatures. The negative ΔH° value (−16.74 kJ/mol) confirmed that adsorption was an exothermic process with the value of ΔH° under −21.9 kJ/mol, verifying that the physisorption mechanism was more dominant than chemisorption.

Table 8. Thermodynamic parameters of the adsorption of RhB on MIL-100(Fe)@TiO_2.

Temperature (K)	Thermodynamic Parameters				
	ln K_d	ΔG^o	ΔH^o	ΔS^o	R^2
303.15	8.0958	−20.4046	−16.7413	12.1974	0.9935
318.15	7.8238	−20.6947			
333.15	7.4964	−20.7636			

3.4. Effect of Variables on Photocatalytic Dye Adsorption—Degradation

3.4.1. Effect of Adsorbent Mass towards Adsorption

The effect of the adsorbent loading on the adsorption capacity was investigated in this study. As shown in Figure 14, the adsorption capacity towards RhB after 60 min increased when the adsorbent dose increased from 10 to 50 mg. This result indicated that more surface area and active sites were available with increasing adsorbent dosage in the adsorption system.

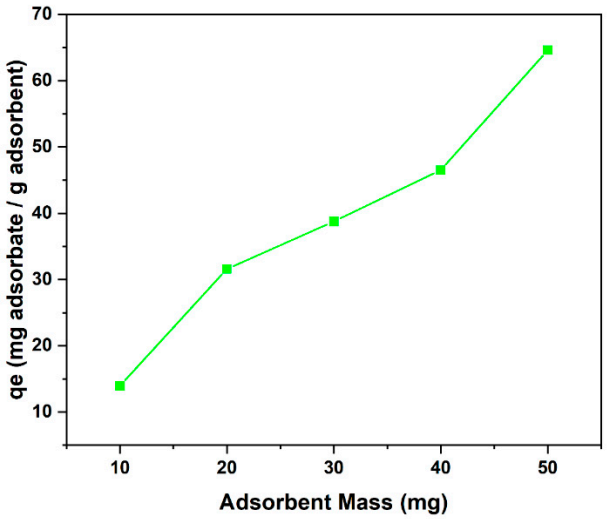

Figure 14. Effect of adsorbent mass towards RhB adsorption.

3.4.2. Effect of Adsorbent Ratio towards Photocatalytic Degradation

Different ratios of the MIL-100(Fe) and TiO_2 in the composite could impact the material's porosity, thus, impacting its transfer efficiency and accessibility of the active sites for photocatalytic degradation. This occurrence was studied by varying the mole ratio of TiO_2 (0.7; 1.4; and 2.4) incorporated into the constant amount of MIL-100(Fe) (denoted as $M_3T_{0.7}$; $M_3T_{1.4}$; and $M_3T_{2.4}$). The suitable amount of TiO_2 inside the composite could enhance the photoreactivity of the composite by increasing the specific surface area and promoting charge transfer [13]. The results of this study are shown in Figure 15. As shown in the figure, $M_3T_{1.4}$ exhibited the best performance on the overall degradation of RhB in the aqueous system. The results also indicated that high TiO_2 content leads to catalyst aggregation, which lowers active sites, and reduces light penetration, and scattering [13].

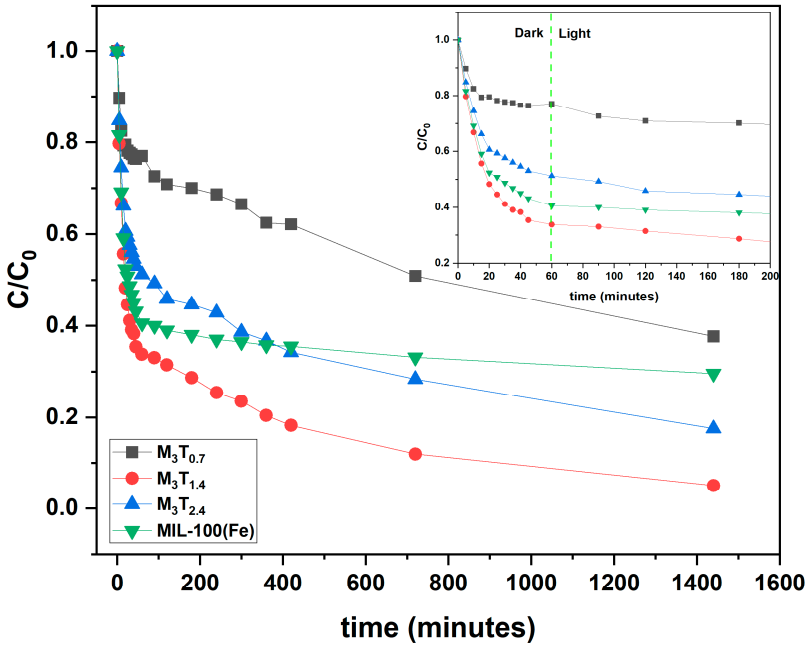

Figure 15. Effect of TiO_2 ratio towards RhB adsorption and photocatalytic degradation.

3.4.3. Effect of Fenton Addition

Adding Fenton reagent (H_2O_2) to the process can enhance the number of •OH species while lowering the radiation intensity, energy consumption, and cost-effectiveness. This phenomenon was studied by adding various amounts of Fenton (1 mL, 2 mL, and 3 mL) into the system containing 100 ppm of RhB and 50 mg of $M_3T_{1.4}$ adsorbent. The photocatalytic degradation process in this research was performed by radiating the solution with the visible LED light after adsorption. The rate constant of the degradation process was determined by non-linear fitting of the experimental data, as shown in Figure 16. Based on the non-linear fitting in Table 8, first-order kinetics suited the experimental data better than the second-order and BMG model kinetics. From the synthesized materials, $M_3T_{1.4}$ exhibited the highest rate constant (k_{1p}), compared with the others. Based on the result shown in Figure 17, adding a small amount of Fenton improved the photodegradation ability, as shown in Figure 17 and Table 9. As previously mentioned, there are three possible ways in which Fenton could create a sufficient amount of $^{\circ}OH$ radicals: (i) it obtains electrons from $^{\circ}O_2^-$ radicals to make the $^{\circ}OH$ radicals; (ii) it reduces H_2O_2 at the band conduction to produce $^{\circ}OH$ radicals, which prevent photo-generated electrons and holes from recombination; or (iii) $^{\circ}OH$ radicals are produced when visible light irradiation causes self-degradation. As a result of these actions, the oxidation rate is accelerated, and the removal efficiency is increased [27].

3.4.4. Reusability Test

The reusability potential of the composite was investigated in this study for five cycles of adsorption–photodegradation of RhB. The experiments were conducted as follows: after adsorption–photodegradation, the adsorbent was soaked in ethanol (24 h), and centrifuged, then dried at 80 °C for 6 h. Subsequently, the adsorbent was used in the next cycle. Based on the results shown in Figure 18, the removal percentage of the RhB slightly decreased after five cycles, indicating the stability of composite as the adsorbent.

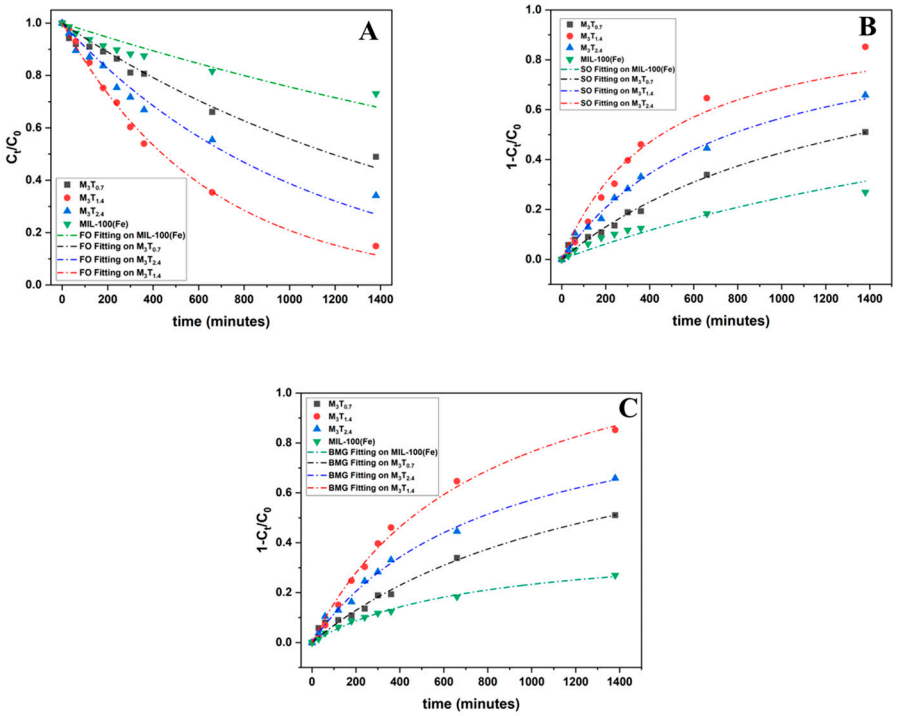

Figure 16. (**A**) FO kinetic fittings on each component; (**B**) SO kinetic fitting on each component; (**C**) BMG kinetic fittings on each component.

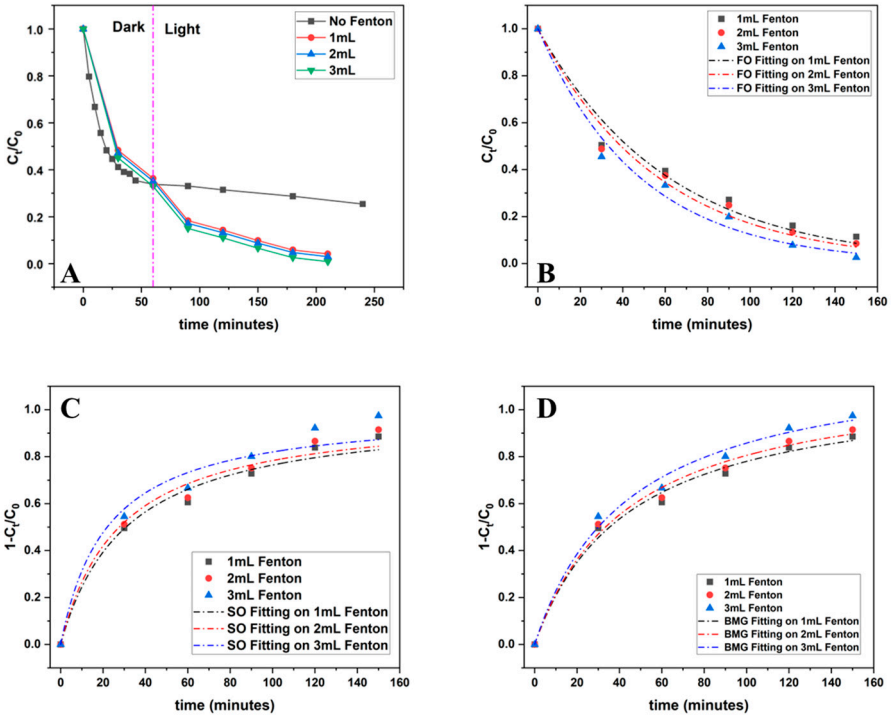

Figure 17. (**A**) Effect of each Fenton volume towards RhB adsorption and photocatalytic degradation (**B**) FO kinetic fittings on each Fenton volume; (**C**) SO kinetic fittings on each Fenton volume; (**D**) BMG kinetic fittings on each Fenton Volume.

Table 9. Photocatalytic degradation kinetic reaction.

Kinetic Reaction Model	Technical Constant [a]	Catalyst and LED Irradiation without Fenton				Catalyst and LED Irradiation with Fenton on $M_3T_{1.4}$		
		$M_3T_{0.7}$	$M_3T_{1.4}$	$M_3T_{2.4}$	MIL-100(Fe)	1 mL	2 mL	3 mL
First-order kinetics $C_t = C_0 \exp(-k_1 t)$	$k_{1p} \times 10^3$ (min^{-1})	0.5834	1.5700	0.9479	0.2793	16.32	17.68	20.84
	R^2	0.9847	0.9944	0.9829	0.9462	0.9914	0.9964	0.9925
Second-order kinetics $1 - \frac{C_t}{C_0} = \frac{k_2 t}{1+k_2 t}$	$k_{2p} \times 10^3 (L \cdot mg^{-1} min^{-1})$	0.7483	2.2100	1.3100	0.3305	32.43	36.17	45.56
	R^2	0.9830	0.9666	0.9629	0.9039	0.9842	0.9795	0.9659
BMG $1 - \frac{C_t}{C_0} = \frac{t}{m+bt}$	m (min)	1,353.4	568.115	783.069	1,819.64	39.26	38.02	35.69
	b	0.9767	0.7399	0.9663	2.4655	0.8896	0.8615	0.8088
	R^2	0.9809	0.9829	0.9832	0.9249	0.9811	0.9891	0.9885

[a] Calculated based on non-linear fitting on Origin Pro 2021 Software (Northampton, MA, USA).

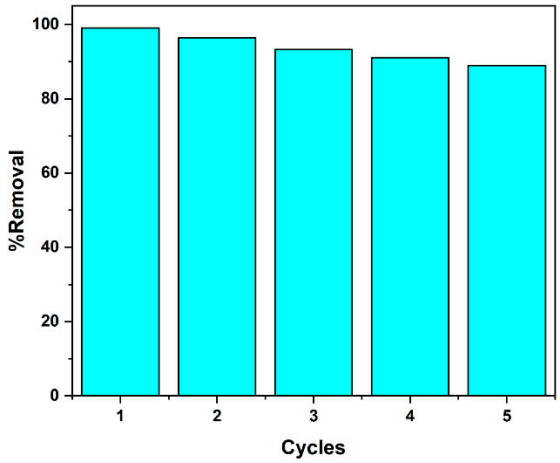

Figure 18. Stability and reusability of $M_3T_{1.4}$.

3.5. Plausible Mechanism of Photocatalytic Degradation of RhB on M_xT_y

During photocatalytic degradation, many active species are involved in the process, such as photoinduced hydroxyl radicals (OH^*), superoxide anion radicals (O_2^{*-}), and electron holes (h^+). Free radical scavenging experiments were conducted to confirm the existence of these active species inside the system. Isopropanol (IP), benzoquinone (BQ), ammonium oxalate (AO), and sodium azide (SA) were prepared with a concentration of 0.001 M as scavengers for OH^*, O_2^{*-}, h^+, and O_2, respectively. RhB degradation was decreased and hindered with the presence of BQ and IP (Figure 19A). RhB only slightly degraded with the addition of AO and SA. The arrangement of total degradation was determined based on the influence of each free radical scavenger: BQ > IP > AO > SA > no scavenger. Briefly, this experiment concluded that the crucial O_2^{*-} active species played a crucial role in the mechanism of RhB degradation.

From the UV-Vis DRS characterization in Table 3, a high band gap value of MIL-100(Fe) (5.35 eV) may restrict the excitation of the electron processes, which decreases its capability in photocatalytic degradation. However, the $M_3T_{1.4}$ composite exhibited the lowest band gap energy value (3.26 eV) compared with the other ratios, including its precursor (pristine MIL-100(Fe) and TiO_2 anatase). These results showed that the $M_3T_{1.4}$ composite successfully improved the photocatalytic degradation capability, corresponding to its lower band gap value. Therefore, a plausible mechanism of photocatalytic degradation has been shown (in Figure 19B), with the further explanation as follows: (1) visible light irradiation gives sufficient energy for the electrons (e^-) from MIL-100(Fe)'s conduction band to jump/migrate into the TiO_2's conduction band; (2) the excitation of the electrons creates holes (h^+) on the TiO_2's valence band, which then migrate into the MIL-100(Fe)'s valence band; (3) this repeating

process allows photo-excited electrons (e^-) and holes (h^+) to contact with oxygen and water molecules, respectively; (4) after contact with photo-excited electrons and holes, oxygen molecules create O_2^{*-} while water molecules create OH^* [8]; (5) these free radicals will then degrade the organic pollutant and turn it into mineralization products, such as carbon dioxide and water.

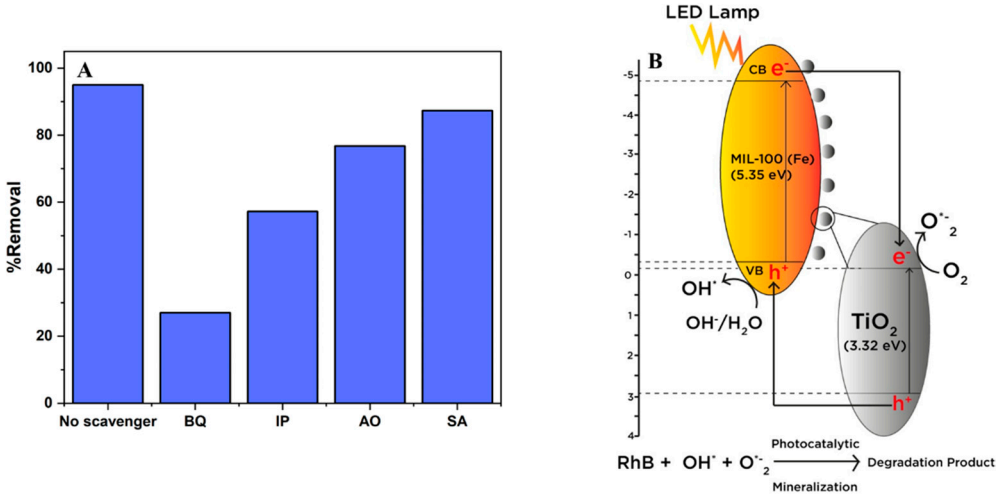

Figure 19. (**A**) Free radicals scavenging experiment on overall degradation; (**B**) plausible mechanism of photocatalytic degradation of RhB towards M_xT_y.

4. Conclusions

In summary, an effective and efficient photocatalyst composite was successfully synthesized via a simple hydrothermal method from MIL-100(Fe) and a TiO_2 anatase precursor. Characterization of the synthesized M_xT_y proved to be quite successful and provided enough evidence to conclude that the materials will have high photocatalytic performances. This was confirmed with the aforementioned adsorption–photocatalytic degradation experiment results, in which the optimal composite ($M_3T_{1.4}$) degraded the organic RhB pollutant to 99%. The addition of Fenton was also proven to be successful in increasing the photocatalytic abilities of the synthesized materials. The synthesized materials were also found to have good reusability.

Author Contributions: Conceptualization, S.I., F.E.S., and V.B.L.; Formal analysis, J.N.P., S.P.S., J.L., H.S. and H.A.; Investigation, P.A. and C.J.W.; Methodology, V.B.L., M.Y., W.I. and P.A.; Validation, S.I., I.G.W., and F.E.S.; Writing—original draft, P.A. and V.B.L.; Writing—review & editing, S.I., J.N.P., S.P.S. All authors have read and agreed to the published version of the manuscript.

Funding: This research was funded by the Directorate of Research and Community Service, Deputy for Strengthening Research and Development, Ministry of Culture and Education, Research and Technology, Number: 260C/WM01.5/N/2022.

Institutional Review Board Statement: Not applicable.

Informed Consent Statement: Not applicable.

Data Availability Statement: All data have been given in this manuscript.

Conflicts of Interest: The authors declare no conflict of interest.

References

1. Al-Maythalony, B.A.; Shekhah, O.; Swaidan, R.; Belmabkhout, Y.; Pinnau, I.; Eddaoudi, M. Quest for anionic MOF membranes: Continuous sod -ZMOF membrane with Co2 adsorption-driven selectivity. *J. Am. Chem. Soc.* **2015**, *137*, 1754–1757. [CrossRef] [PubMed]
2. Lu, G.; Chu, F.; Huang, X.; Li, Y.; Liang, K.; Wang, G. Recent advances in Metal-Organic Frameworks-based materials for photocatalytic selective oxidation. *Coord. Chem. Rev.* **2022**, *450*, 214240. [CrossRef]

3. Wang, M.; Yang, L.; Guo, C.; Liu, X.; He, L.; Song, Y.; Zhang, Q.; Qu, X.; Zhang, H.; Zhang, Z.; et al. Bimetallic Fe/Ti-Based Metal–Organic Framework for Persulfate-Assisted Visible Light Photocatalytic Degradation of Orange II. *ChemistrySelect* **2018**, *3*, 3664–3674. [CrossRef]
4. Ai, L.; Zhang, C.; Li, L.; Jiang, J. Iron terephthalate metal-organic framework: Revealing the effective activation of hydrogen peroxide for the degradation of organic dye under visible light irradiation. *Appl. Catal. B Environ.* **2014**, *148–149*, 191–200. [CrossRef]
5. Li, X.; Guo, W.; Liu, Z.; Wang, R.; Liu, H. Fe-based MOFs for efficient adsorption and degradation of acid orange 7 in aqueous solution via persulfate activation. *Appl. Surf. Sci.* **2016**, *369*, 130–136. [CrossRef]
6. Liu, N.; Huang, W.; Zhang, X.; Tang, L.; Wang, L.; Wang, Y.; Wu, M. Ultrathin graphene oxide encapsulated in uniform MIL-88A(Fe) for enhanced visible light-driven photodegradation of RhB. *Appl. Catal. B Environ.* **2018**, *221*, 119–128. [CrossRef]
7. Ke, F.; Wang, L.; Zhu, J. Facile fabrication of CdS-metal-organic framework nanocomposites with enhanced visible-light photocatalytic activity for organic transformation. *Nano Res.* **2015**, *8*, 1834–1846. [CrossRef]
8. Huang, J.; Song, H.; Chen, C.; Yang, Y.; Xu, N.; Ji, X.; Li, C.; You, J.A. Facile synthesis of N-doped TiO_2 nanoparticles caged in MIL-100(Fe) for photocatalytic degradation of organic dyes under visible light irradiation. *J. Environ. Chem. Eng.* **2017**, *5*, 2579–2585. [CrossRef]
9. He, X.; Fang, H.; Gosztola, D.J.; Jiang, Z.; Jena, P.; Wang, W.N. Mechanistic Insight into Photocatalytic Pathways of MIL-100(Fe)/TiO 2 Composites. *ACS Appl. Mater. Interfaces* **2019**, *11*, 12516–12524. [CrossRef]
10. Liu, L.; Liu, Y.; Wang, X.; Hu, N.; Li, Y.; Li, C.; Meng, Y.; An, Y. Synergistic effect of B-TiO_2 and MIL-100(Fe) for high-efficiency photocatalysis in methylene blue degradation. *Appl. Surf. Sci.* **2021**, *561*, 149969. [CrossRef]
11. Kondamareddy, K.K.; Neena, D.; Lu, D.; Peng, T.; Lopez MA, M.; Wang, C.; Yu, Z.; Cheng, N.; Fu, D.J.; Zhao, X.Z. Ultra-trace (parts per million-ppm) W 6+ dopant ions induced anatase to rutile transition (ART) of phase pure anatase TiO 2 nanoparticles for highly efficient visible light-active photocatalytic degradation of organic pollutants. *Appl. Surf. Sci.* **2018**, *456*, 676–693. [CrossRef]
12. Horcajada, P.; Surblé, S.; Serre, C.; Hong, D.Y.; Seo, Y.K.; Chang, J.S.; Grenèche, J.M.; Margiolaki, I.; Férey, G. Synthesis and catalytic properties of MIL-100(Fe), an iron(III) carboxylate with large pores. *Chem. Commun.* **2007**, *100*, 2820–2822. [CrossRef]
13. Angela, S.; Bervia Lunardi, V.; Kusuma, K.; Edi Soetaredjo, F.; Nyoo Putro, J.; Permatasari Santoso, S.; Elisa Angkawijaya, A.; Lie, J.; Gunarto, C.; Kurniawan, A.; et al. Facile Synthesis of Hierarchical Porous ZIF-8@TiO_2 for Simultaneous Adsorption and Photocatalytic Decomposition of Crystal Violet. *Environ. Nanotechnol. Monit. Manag.* **2021**, *16*, 100598. [CrossRef]
14. Guo, S.; Chi, L.; Zhao, T.; Nan, Y.; Sun, X.; Huang, Y.; Hou, B.; Wang, X. Construction of MOF/TiO_2 nanocomposites with efficient visible-light-driven photocathodic protection. *J. Electroanal. Chem.* **2021**, *880*, 114915. [CrossRef]
15. Zheng, J.; Liu, Z.; Liu, X.; Yan, X.; Li, D.; Chu, W. Facile hydrothermal synthesis and characteristics of B-doped TiO_2 hybrid hollow microspheres with higher photocatalytic activity. *J. Alloy. Compd.* **2011**, *509*, 3771–3776. [CrossRef]
16. Xu, J.; Xu, J.; Jiang, S.; Cao, Y.; Xu, K.; Zhang, Q.; Wang, L. Facile synthesis of a novel Ag3PO4/MIL-100(Fe) Z-scheme photocatalyst for enhancing tetracycline degradation under visible light. *Environ. Sci. Pollut. Res.* **2020**, *27*, 37839–37851. [CrossRef]
17. Tian, H.; Araya, T.; Li, R.; Fang, Y.; Huang, Y. Removal of MC-LR using the stable and efficient MIL-100/MIL-53 (Fe)photocatalyst: The effect of coordinate immobilized layers. *Appl. Catal. B Environ.* **2019**, *254*, 371–379. [CrossRef]
18. Wei, Y.; Cheng, G.; Xiong, J.; Xu, F.; Chen, R. Positive $Ni(HCO_3)_2$ as a Novel Cocatalyst for Boosting the Photocatalytic Hydrogen Evolution Capability of Mesoporous TiO_2 Nanocrystals. *ACS Sustain. Chem. Eng.* **2017**, *5*, 5027–5038. [CrossRef]
19. Giles, C.H.; MacEwan, T.H.; Nakhwa, S.N.; Smith, D. Studies in Adsorption. Part XI.* A System. *J. Chem. Soc.* **1960**, *846*, 3973–3993. [CrossRef]
20. Bonilla-Petriciolet, A.; Mendoza-Castillo, D.I.; Reynel-Ávila, H.E. Adsorption processes for water treatment and purification. In *Adsorption Processes for Water Treatment and Purification*; Springer: Berlin/Heidelberg, Germany, 2017. [CrossRef]
21. Lima, E.C.; Hosseini-Bandegharaei, A.; Moreno-Piraján, J.C.; Anastopoulos, I. A critical review of the estimation of the thermodynamic parameters on adsorption equilibria. Wrong use of equilibrium constant in the Van't Hoof equation for calculation of thermodynamic parameters of adsorption. *J. Mol. Liq.* **2019**, *273*, 425–434. [CrossRef]
22. Karmakar, S.; Roy, D.; Janiak, C.; De, S. Insights into multi-component adsorption of reactive dyes on MIL-101-Cr metal-organic framework: Experimental and modeling approach. *Sep. Purif. Technol.* **2019**, *215*, 259–275. [CrossRef]
23. Yadav, S.; Asthana, A.; Singh, A.K.; Chakraborty, R.; Vidya, S.S.; Susan, M.A.B.H.; Carabineiro, S.A. Adsorption of cationic dyes, drugs and metal from aqueous solutions using a polymer composite of magnetic/β-cyclodextrin/activated charcoal/Na alginate: Isotherm, kinetics and regeneration studies. *J. Hazard. Mater.* **2021**, *409*, 124840. [CrossRef] [PubMed]
24. Biggar, J.; Cheung, M. Adsorption of picloram (4-amino-3,5,6-trichloropicolinic acid) on panoche, ephrata, and palouse soils: A thermodynamic approach to the adsorption mechanism. *Soil Sci. Soc. Am. J.* **1973**, *37*, 863–868. [CrossRef]
25. Khan, A.A.; Singh, R. Adsorption thermodynamics of carbofuran on Sn (IV) arsenosilicate in H^+, Na^+ and Ca^{2+} forms. *Colloids Surf.* **1987**, *24*, 33–42. [CrossRef]
26. Milonjić, S.K. A consideration of the correct calculation of thermodynamic parameters of adsorption. *J. Serbian Chem. Soc.* **2007**, *72*, 1363–1367. [CrossRef]
27. Hejazi, R.; Mahjoub, A.R.; Khavar AH, C.; Khazaee, Z. Fabrication of novel type visible-light-driven TiO_2@MIL-100 (Fe) microspheres with high photocatalytic performance for removal of organic pollutants. *J. Photochem. Photobiol. A Chem.* **2020**, *400*, 112644. [CrossRef]